Corrosion Science 184 (2021) 109397

Contents lists available at ScienceDirect

Corrosion Science

journal homepage: www.elsevier.com/locate/corsci

Ni coatings for corrosion protection of Mg alloys prepared by an in-situ micro-forging assisted cold spray: Effect of powder feedstock characteristics

Ying-Kang Wei [a], Xiao-Tao Luo [a,*], Xin Chu [c], Yi Ge [a], Guo-Sheng Huang [b,*], Ying-Chun Xie [d], Ren-Zhong Huang [d], Chang-Jiu Li [a]

[a] State Key Laboratory for Mechanical Behavior of Materials, School of Materials Science and Engineering, Xi'an Jiaotong University, Xi'an, Shaanxi, 710049, PR China
[b] State Key Laboratory for Marine Corrosion and Protection, Luoyang Ship Material Research Institute (LSMRI), Qingdao, Shandong, 266237, PR China
[c] Department of Mining and Materials Engineering, McGill University, Montreal, Quebec, H3A 0C5, Canada
[d] The Key Lab of Guangdong for Modern Surface Engineering Technology, Guangdong Institute of New Materials, Guangzhou, 510651, PR China

ARTICLE INFO

Keywords:
Magnesium alloy
Nickel coating
Cold spray
Powder characteristics
In-situ micro-forging
Corrosion performance

ABSTRACT

Three nickel (Ni) powders, i.e. gas-atomized spherical Ni (GA-Ni), carbonyl irregular Ni (C-Ni), and electrolytic dendritic porous Ni (E-Ni), were sprayed on magnesium alloys by an in-situ micro-forging assisted cold spray method. Although all deposited coatings present extremely low porosity, the C-Ni and E-Ni coatings reveal poorer inter-particle bonding than GA-Ni coating. Electrochemical tests reveal that the inter-particle gaps will act as fast pathways for the corrosive media to penetrate the coatings, thereby the GA-Ni coating with intimate inter-particle boundaries can isolate the corrosive media for 3000 h and the C-Ni and E-Ni coatings fail after <10 h corrosion.

1. Introduction

Magnesium (Mg) and its alloys have wide applications in various industries including automotive, aerospace, military, communication and biomedicine due to their excellent properties such as low density, high specific strength, high thermal conductivity and good biocompatibility [1,2]. However, their high vulnerability to corrosion attack in humid and aqueous environments due to the mild protection from their inhomogeneous and poorly bonded native oxide/hydroxide films hinders their further applications [1]. Although various surface modification techniques are available which might improve the surface properties of Mg alloys [3,4], the existing techniques are limited either by performance, cost or environmental pollution hazards. Cold spray (CS), as an emerging coating process, could potentially be a facile and green technique for surface protection of Mg alloys [5–7].

In CS, micron-sized ductile particles are accelerated in a compressed gas stream to supersonic velocities (300−1200 m s^{-1}) and the solid state impact on the metallic substrate generates metallurgical bonding and/or mechanical interlocking to form coatings [8]. In recent years, aluminium (Al) based coatings have been frequently deposited on Mg substrates by CS for corrosion protection [6,9–11]. For example, Tao et al. [9] and Diab et al. [10] prepared compact pure Al and Al alloy coatings on Mg alloys, respectively, and the coatings are capable to completely prevent aqueous corrosive media from permeating. However, due to their relatively low intrinsic corrosion resistance, Al based materials usually cannot survive extremely severe corrosive environments. Nickel (Ni), as a metal with excellent corrosion resistance even in extremely severe corrosive environments, is another accepted candidate for corrosion protection coatings of Mg alloys [12,13]. So far, CS Ni-based coatings (using gas atomized spherical Ni (GA-Ni) powders) for corrosion protection have been reported by many researchers [14–17]. However, it was found that the corrosion protection performance of these coatings is unsatisfactory. For instance, local corrosion spots were detected at interfaces of CS Ni coating and steel substrate after only 48 h exposure in salt fog [15]. Generally, the poor corrosion protection performance is caused by the CS coating defects, i.e. interconnected pores and gaps, which are usually observed in conventional CS Ni coating and act as fast penetrating channels for corrosive media. In cold sprayed metallic coatings, the inter-particle bonding quality and porosity level are determined by the degree of particle plastic deformation during deposition. Large plastic deformation is always needed to produce a dense coating. Usually, using helium (He) as the propellant gas or increasing nitrogen (N_2) gas pressure and temperature will achieve higher particle velocity and larger plastic deformation of the deposited

* Corresponding authors.
E-mail addresses: luoxiaotao@mail.xjtu.edu.cn (X.-T. Luo), huanggs@sunrui.net (G.-S. Huang).

https://doi.org/10.1016/j.corsci.2021.109397
Received 19 November 2020; Received in revised form 10 March 2021; Accepted 13 March 2021
Available online 16 March 2021

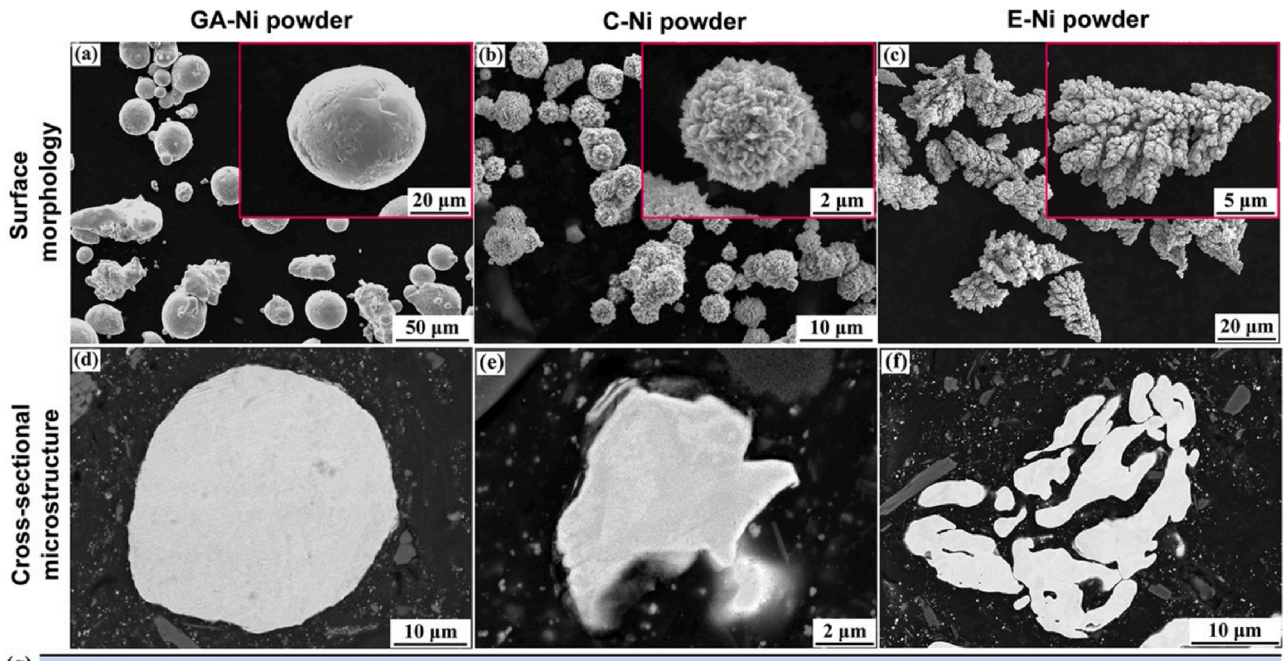

(g)

Powders	Surface morphology		Cross-sectional microstructure	Size distribution		
	Shape	Surface features		D10/μm	D50/μm	D90/μm
GA-Ni	Spherical	Smooth	Dense	7.1	31.7	50.7
C-Ni	Irregular	~0.1 μm protruding granules	Dense	0.1	5.1	9.6
E-Ni	Dendritic	~0.5-1 μm protruding granules	Porous	5.84	27.3	42.3

Fig. 1. Surface morphologies and cross-sectional microstructures of GA-Ni (a and d), C-Ni (b and e) and E-Ni (c and f) powders; inset in (a) to (c) is the morphologies of GA-Ni, C-Ni and E-Ni in high magnification, respectively. (g) summarized the surface morphologies, cross-sectional microstructures and size distributions of these powders.

particles and thus lead to more compact coatings [18]. However, He gas is expensive and nonrenewable and high N_2 gas temperature could deteriorate the Mg alloy substrate's microstructure [19]. In our previous studies [20–22] we have developed a novel in-situ micro-forging assisted cold spray process (MF-CS), which can effectively improve the density of metallic coatings without using costly He gas or very high N_2 gas temperature. The main feature of the MF-CS process is to spray a mixture of large-sized micro-forging (MF) particles (150−300 μm) and coating materials powders. During spray, large MF particles having high kinetic energies in-situ forge and further compact the exposed porous coating layer (in-situ MF effect), after which they rebound off without contaminating the coating materials. Our previous studies have shown that the MF-CS can be a viable method to achieve high density (porosity: < 0.3 %) corrosion resistant Ni coatings on AZ31B Mg alloys using GA-Ni powder [23].

Besides the spraying process setup/parameters, the powder feedstock characteristics (e.g. size distributions, morphologies and microstructures) also prove critical in determining the coating quality and production cost. In addition to the expensive atomization process, Ni powders can also be manufactured by low-cost routes, e.g. fine carbonyl nickel (C-Ni) and non-spherical electrolytic nickel (E-Ni) (the unit prices of both powders are less than half of the GA-Ni powder). Many researchers [24–29] investigated the effect of powder characteristics on the particle acceleration and deposition behavior (e.g. deposition efficiency (DE)). It has been demonstrated that spraying powders with fine, irregular morphology and porous microstructure usually results in better DE. Generally, increasing the impact velocity or decreasing the critical velocity will lead to higher DE [30]. On the one hand, compared with larger and/or spherical powders, smaller and/or irregular shape powders could obtain higher particle impact velocity in cold spray [27]. On the other hand, porous powders usually exhibit lower critical velocity due to the lower yield stress under both static and dynamic loadings as compared to solid counterparts [31]. Many previous studies [32–34] reported that irregular/porous powders revealed higher DE than spherical powder (under similar CS conditions) and thus this expects to reduce the feedstock cost during production. However, it is understood that a high feedstock DE does not necessarily lead to high coating quality, e.g. porosity and inter-particle bonding state. For instance, Chu et al. [28] have shown that the irregular particle morphology will facilitate the formation of inter-particle bonding due to the localized shear deformation at the particle boundaries and thus mechanical anchorage effects. However, pores are frequently observed in these CS coatings deposited with irregular metallic powders [25]. The comprehensive effect of powder characteristics on the quality of CS coatings is complicated and currently limited studies have systematically investigated the cold sprayed coating microstructure and corrosion protection performance using C-Ni and E-Ni powders.

In this study, three commercial Ni powders (GA-Ni, C-Ni and E-Ni) were used as the feedstock powders to produce Ni coatings on AZ31B Mg alloy substrates via the MF-CS process under the same spraying condition. The coating microstructures and adhesion strengths were characterized and are compared. Electrochemical corrosion performance and long-term static immersion corrosion performance are evaluated. The corrosion protection performance was correlated with the coating microstructure and feedstock characteristics. The purpose of this study is to unveil the relationship between feedstock powder characteristics, coating microstructure and corrosion performance and ultimately guide cold spray industrial applications.

Table 1
Chemical compositions of GA-Ni, C-Ni and E-Ni powders (wt.%).

Powder	Fe	C	S	Co	O	Ni
GA-Ni	0.04	0.03	0.02	0.05	0.1	
C-Ni	0.01	0.15	0.01	0.005	0.2	Remainder
E-Ni	0.006	0.08	0.003	0.005	0.13	

2. Experiments

2.1. Materials

Commercially available gas atomized Ni (GA-Ni, ~ USD 70/kg), carbonyl Ni (C-Ni, ~ USD 30/kg) and electrolytic Ni (E-Ni, ~ USD 30/kg) powders (BGRIMM Co., Ltd., Beijing, China) were used as feedstock powders. As seen from Fig. 1a, GA-Ni particles present a spherical shape with smooth surface. Non-spherical C-Ni (irregular shape) with 0.1 μm surface protruding granules and dendritic E-Ni with 0.5–1 μm loosely packed grains can be clearly observed in Fig. 1b and c, respectively. Fig. 1d-1f reveal the polished cross-sectional microstructure of these Ni powders. As shown, both GA-Ni (Fig. 1d) and C-Ni (Fig. 1e) particles present a dense microstructure, while inter-granular spacings can be clearly observed in E-Ni (Fig. 1f) particles which indicate the porous microstructure. Moreover, the D50 values of GA-Ni, C-Ni and E-Ni powders were measured to be 31.7, 5.1 and 27.3 μm, respectively. Fig. 1g summarized the surface morphology, cross-sectional microstructure and size distribution of the three types of Ni powders. The chemical compositions of these Ni powders are listed in Table 1. It should be pointed out that the oxygen content of the feedstock particles will affect the quality of inter-particle bonding of CS coatings [35]. In this work, the similar oxygen content of the three Ni powders ensures the consistency of the influence of oxygen content on the quality of inter-particle bonding. 40 vol.% commercial spherical martensitic 410 stainless steel (SS) powders (size range 150–200 μm) (Wei Guang Shot-peening material Co., Ltd. Wuxi, China) were mechanically mixed with each Ni powder to introduce sufficient in-situ MF effect [23]. The powder mixtures were sealed in a plastic container and then admixed using a tumbler for 2 h at a rotation speed of 40 rpm. Then the mixtures were dried at 75 °C for 1 h in an electrical oven and vacuum sealed for cold spray. Actually, fracturing and/or cold-welding of metallic particles are often observed during the ball milling process. In this work, a gently mixing method was used in a low energy drum miller. Not any conventional milling balls with diameters of millimeter were added. Therefore, obvious fracture and/or cold-welding will not happen for Ni powders after the mixing process. Commercial AZ31B magnesium alloy plates were cut into dimensions of 100 mm × 100 mm × 4 mm and are used as substrates. Prior to deposition, substrates were cleaned for 10 min in an ultrasonic acetone bath, and then sandblasted with 24 mesh bronze corundum grits using 0.6 MPa pressure to remove the scale and roughen the surface (Ra of ~ 10 μm) to obtain better adhesion.

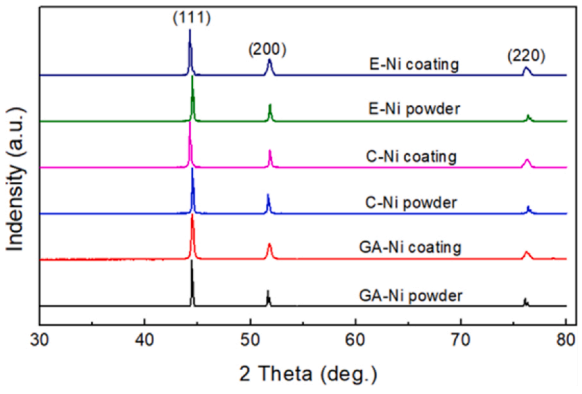

Fig. 2. X-ray diffraction patterns of C-Ni, E-Ni and GA-Ni powders and their corresponding MF-CS coatings.

2.2. Coating deposition

In this study, an in-house built high-pressure cold spray system (CS2000, Xi'an Jiaotong University) was used. This system operates using an optimized De-Laval nozzle with a throat diameter of 2.4 mm, an outlet diameter of 6.25 mm and a divergence length of 200 mm. A 120 mm long preheating chamber is fixed before the De-Laval nozzle so that powders can be preheated to approximately the gas temperature before entering the nozzle. For all samples, N_2 was used as the propellant gas. The process parameters were optimized to avoid the contamination of MF particles and a gas preheating temperature of 400 °C and a gas pressure of 2.5 MPa were finally selected. The stand-off distance and traverse speed of the spray torch were set at 20 mm and 100 mm/s, respectively. The mixed powders (Ni + SS powders) were sprayed at a feed rate of 20 g min^{-1} and ~300 μm thick coatings were produced per sample. For brevity, the GA-Ni coated AZ31B, C-Ni coated AZ31B and E-Ni coated AZ31B are referred to as "GA-Ni coating", "C-Ni coating" and "E-Ni coating", respectively, in following sections. After the MF-CS process, Ni coating specimens with dimensions of 25 mm × 15 mm × 4 mm were sectioned, ground to the thickness of 150–200 μm, finely polished with 0.05 μm colloidal silica suspension, ultrasonic cleaned in acetone, and dried in air.

2.3. Characterization

The volumetric particle size distributions of Ni powders were measured by a laser particle size analyzer (LA-920, Horiba, Tokyo, Japan). The phase compositions of Ni powders and coatings were analyzed with an X-ray diffraction analyzer (XRD, D8 ADVANCE, BRUKER, Germany) using Cu Kα radiation in the angle range from 30° to 80° and the step of 0.02°. The morphologies of Ni powders and microstructures of as-sprayed and as-corroded Ni coatings were characterized using a field emission scanning electron microscope (SEM, MIRA3 LMH, TESCAN, Czech) attached with an energy dispersive spectrometer (EDS, Oxford Instruments, UK) system and an optical microscope. To avoid corrosion of coating/substrate interfaces during SEM sample preparations, absolute ethanol-based polishing agent was used in both grinding and polishing processes. The coating porosity was estimated based on 15 backscattered electron (BSE) images of as-deposited coatings at 1000× magnification using ImageJ software. An Instron material testing machine (INSTRON 5969, Illinois Tool Works Inc., USA) was used to evaluate the adhesion strength of the Ni coatings and five samples per coating were tested in accordance with the ASTM C633-13 standard [36]. All samples were prepared by spraying ~0.15–0.2 mm thick coatings on the top flat surface of AZ31B cylinder coupons with the diameter of 25.4 mm. E-7 adhesive (HUAYI Resins Co., Ltd., Shanghai, China) was used to glue the counter slug.

2.4. Electrochemical measurements

Prior to tests, Ni coating specimens were sealed by epoxy resin with an exposed area of 1 cm^2. The electrochemical measurements were performed using a conventional three-electrode cell where the samples were immersed in 0.6 mol L^{-1} NaCl solution (pH 7, 25 ± 3 °C) and simultaneously connected to a VSP electrochemical workstation (Bio-Logic Science Instruments, France) as a working electrode. A saturated calomel electrode (SCE) and platinum plate were used as the reference and counter electrode, respectively. In CS coatings, the gaps between poorly bonded particles usually act as the fast pathway for the corrosive media to penetrate into the coating and the in-depth penetration rate of the corrosive media is determined by the number of connected inter-particle gaps or pores [15]. It suggests that penetration of the corrosive media is a gradual process and thus the electrochemical tests lasting

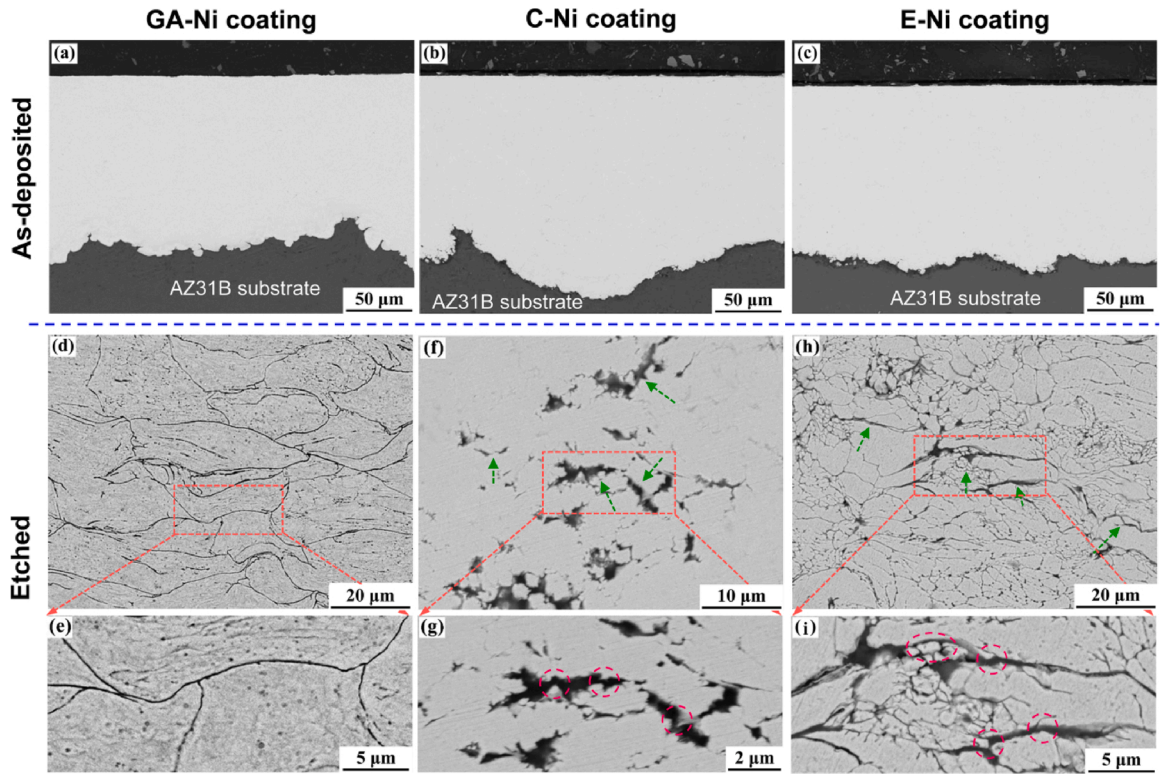

Fig. 3. As-deposited and etched cross-sectional microstructures of the GA-Ni (a and d), C-Ni (b and f) and E-Ni (c and h) coatings. (e), (g) and (i) are the closer views of (d), (f) and (h), respectively.

for only several hours might be not enough to represent the actual corrosion resistance of the coatings. Therefore, in this work, long-term electrochemical corrosion behaviors were tested up to 200−3000 h. Open circuit potential (E_{OCP}) was detected for every 1 min in the first 24 h immersion and for every 1 h in the remaining period. Electrochemical impedance spectroscopy (EIS) was measured at the corresponding E_{OCP} using an alternating sine signal with the amplitude of 10 mV. The measured frequency range was from 100 kHz to 10 mHz and the total number of measured points is 70. The electrochemical results were then analyzed by EC-Lab® and ZSimpWin software. At least 3 replicates were performed to ensure the repeatability of the electrochemical test results.

3. Results and discussion

3.1. Microstructures

3.1.1. XRD patterns of powders and coatings

Fig. 2 shows the XRD patterns of the Ni powders and the corresponding MF-CS coatings. In all cases, diffraction peaks of oxide phases were not identified on the Ni coatings, suggesting no serious oxidation of Ni powders during spray. This is attributed to the low process temperature and very short heating time during the MF-CS process. However, the XRD patterns of Ni phase show an obvious peak broadening after the MF-CS process. The XRD peak broadening in CS Ni coatings as compared to the initial feedstock arises from the grain refinement and multiplication of dislocation induced by severe plastic deformation [18]. In addition, the full width at half maximum (FWHM) of all peaks of the GA-Ni, C-Ni and E-Ni powders increased to 207 ± 54 %, 231 ± 61 % and 246 ± 43 % after spray, respectively. It should be noted that the although the values of the increment of FWHM can not be used for quantitative comparison the degree of plastic deformation of deposited GA-Ni, C-Ni and E-Ni particles due to the high deviation, it still could be expected that the impact velocities of both the fine C-Ni and non-spherical E-Ni particles are higher than that of coarse GA-Ni spherical particles and therefore contribute to the more intensive plastic deformation according to the increase in average value of FWHM. In cold spray, for the same powder material, higher impact velocity suggests higher kinetic energy imparted from the gas stream to deform the particles via the high-velocity impact.

3.1.2. Coating microstructures

Fig. 3 shows the cross-sectional microstructures of the MF-CS Ni coatings produced with different Ni powders. There are generally two main types of defects in conventional cold sprayed coatings: i) pores at the triple particle junctions or particle interior (when using porous powder); and ii) gaps at the poorly bonded inter-particle boundaries which are mainly attributed to the insufficient plastic deformation of sprayed particles during deposition [8]. In this work, no obvious pores can be detected in the 500× magnification photos of polished cross sections of all coatings (Fig. 3a-c). The porosities of the GA-Ni, C-Ni and E-Ni coatings measured by image analysis for 1000× magnification photos (Fig. S1-S3) are as low as 0.21 ± 0.07 %, 0.3 ± 0.1 % and 0.25 ± 0.09 %, respectively. Besides, stainless steel MF particles were not observed in any coatings, which can be explained by the spherical morphology and relatively low impact velocity of the MF particles [20,21,23]. Moreover, the SEM-BSE images confirm that the thickness of the coatings is all about 150−200 μm after fine polishing. Overall, the above results show that MF-CS process can produce extremely low porosity Ni coatings no matter what type of Ni powders was used.

To investigate the inter-particle bonding quality in these Ni coatings, the polished cross sections of the as-deposited coatings were slightly etched in 50 % aqua regia for 1 min to reveal the inter-particle boundaries and then observed by SEM at a high magnification. From the etched cross sections shown in Fig. 3d, intimate inter-particle boundaries (dark lines) can be clearly observed, suggesting excellent inter-particle bonding between the GA-Ni particles. However, many small inter-particle gaps (marked by arrows), which are invisible in the as-deposited coatings, can be found in etched C-Ni (Fig. 3f) and E-Ni

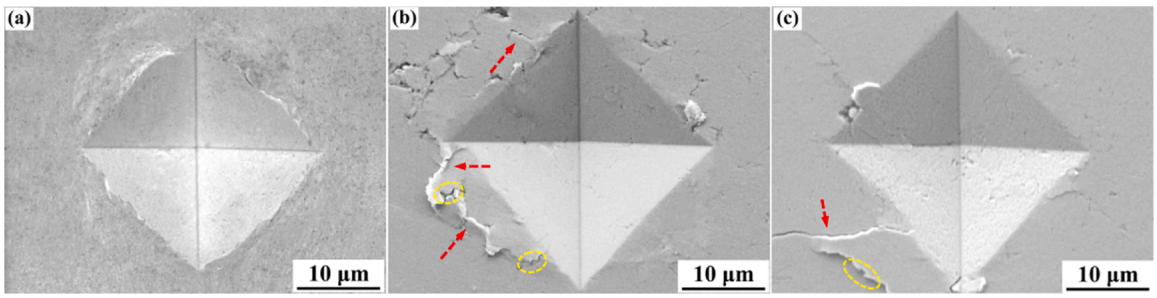

Fig. 4. The cross-sectional microstructures (near the indent) of the GA-Ni (a), C-Ni (b) and E-Ni (c) coatings after microindentation.

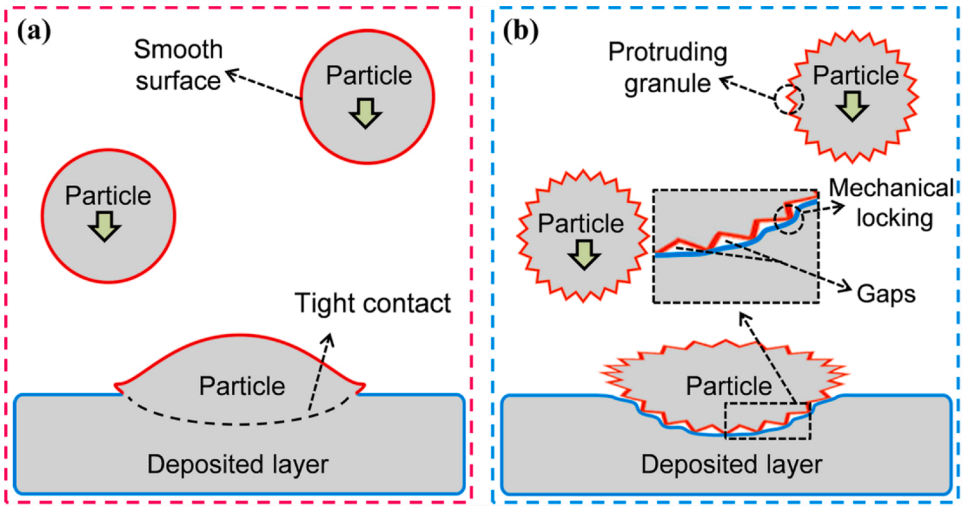

Fig. 5. Schematic illustration of the effect of surface protruding granules on the inter-particle bonding quality of deposited MF-CS particles.

(Fig. 3h) coatings, suggesting relatively poor inter-particle bonding. Moreover, from the closer view of the inter-particle boundaries shown in Fig. 3e, g and i, it is obvious that the deposited Ni particles still retain their surface features from the feedstock particles (inset of Fig. 1a-c): smooth GA-Ni particles (Fig. 3e) (except at the triple particle junction) and rough C-Ni (Fig. 3g) and E-Ni (Fig. 3i) particles (surface protruding granules were denoted by the dashed line ellipses). In MF-CS process, more MF powder will introduce stronger in-situ MF effect and thus larger plastic deformation and higher quality of inter-particle bonding [37]. However, some inter-particle gaps can be still observed in the etched cross sections of C-Ni and E-Ni coatings (Fig. S4) even the MF powders content increased to 70 vol.%. Furthermore, as compared with etched GA-Ni and C-Ni coatings, many grey lines can be observed in etched E-Ni coating, which should be classified as inter-granular boundaries. Besides, some inter-granular spacing can be still detected in the etched E-Ni coating.

To further compare the quality of inter-particle bonding of the MF-CS Ni coatings, microindentation was applied on well-polished cross-sections using Vickers indenter with a load of 200 g and dwelling time of 30 s. Indentation method was commonly used to qualitatively determine the fracture toughness of brittle materials as well as thermal spray ceramic coatings [38]. The crack length after indent is measured, and the longer the crack length, the lower the fracture toughness. In cold or thermal spray coatings, inter-particle boundaries are usually the weakest sites and cracks will initiate and propagate through. From this perspective, the indentation method can somewhat qualitatively evaluate the inter-particle bonding quality [39]. Fig. 4 presents the cross-sectional microstructures (near the indent) of the Ni coatings after microindentation. As compared with the GA-Ni coating (Fig. 4a), cracks as marked by arrows were clearly observed around the indent in the C-Ni (Fig. 4b) and E-Ni (Fig. 4c) coatings. Meanwhile, these cracks also show obvious jagged features (denoted by dashed line ellipses), similar to the bonded interfaces of the deposited C-Ni (Fig. 3g) and E-Ni particles (Fig. 3i), suggesting the inter-particle fracture has occurred during indentation. Therefore, it can be concluded that the deposited GA-Ni particles revealed much better inter-particle bonding than deposited C-Ni and E-Ni particles.

Generally, inter-particle bonding quality in CS is conceived to positively relate to the degree of plastic deformation of deposited particles [8]. However, in this work, the slightly higher deformed C-Ni and E-Ni particles didn't result in better or even same levels of inter-particle bonding as compared with the GA-Ni particles. This anomalous phenomenon may be attributed to the rougher surface of C-Ni and E-Ni powders than GA-Ni powder. A schematic diagram showing the effect of surface protruding granules on the bonding state of deposited Ni particles, based on the detailed microstructure characterization of coatings and results reported by other researchers [40], is displayed in Fig. 5. For simplicity, the sprayed particles were assumed to present spherical shape and dense microstructure. As the feedstock impacts on the previously deposited layers, the interfacial region (especially near the particle edge area) will be extremely compressed and stretched during the plastic deformation [18]. As shown in Fig. 5a, under very high strains, the smooth surface ensures tight contact between sprayed particles and previously deposited layer. By contrast, for rough particles, the surface protruding granules will preferentially contact with previously deposited layer and increase the local deformation at the contact area (Fig. 5b). This phenomenon will promote the formation of mechanical interlocking between the sprayed particles and thus some limitedly deformed particles could be deposited (i.e. increase of deposition efficiency (DE)). Al-Hamdani et al. [40] reported that the DE of aluminum alloy powder increased about ~12 % when fine titanium carbide powders were attached to the substrate surface (satellite

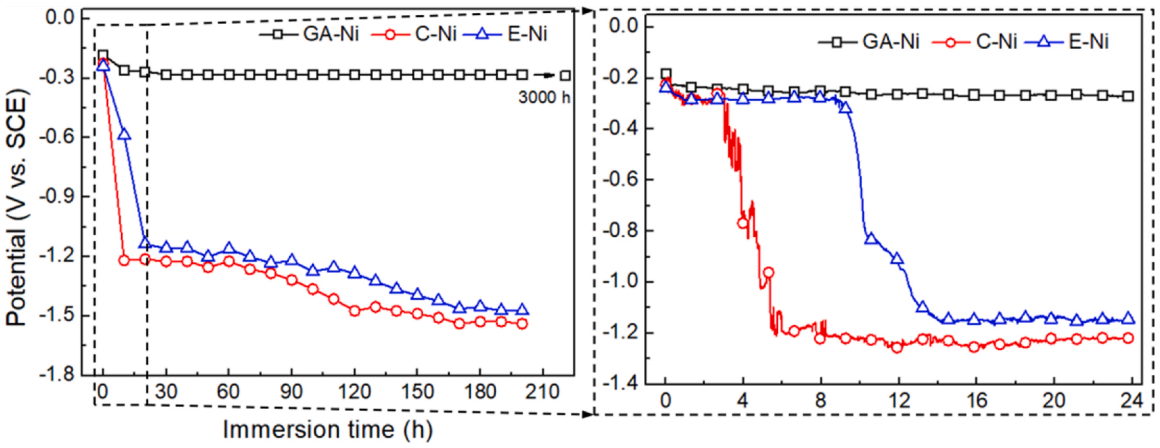

Fig. 6. E_{OCP} vs. time curves of the MF-CS Ni coatings in 0.6 mol L^{-1} NaCl aqueous solution.

structured powder). However, the existences of surface protrusions will inevitably prevent further contact between other surface regions with previously deposited layer and thus small inter-particles gaps will be formed. In this case, it is reasonable that the interfaces with intimate contact are easier to be achieved in MF-CS Ni coating by using smooth GA-Ni powder as compared to rough C-Ni and E-Ni powders. The C-Ni and E-Ni coatings reveal poorer inter-particle bonding than GA-Ni coating due to their rougher particle surfaces.

3.2. Adhesion strength

Higher adhesion strength between coating and substrate ensures the coating to maintain structural integrity much better during service. Generally, the structural integrity is the prerequisite for the corrosion resistance of coatings [17]. The adhesion strength values of the GA-Ni, C-Ni and E-Ni coatings on Mg substrate are similar, which were measured as 65 ± 4 [23], 62 ± 4 and 66 ± 3 MPa, respectively. Further examination of the failed surfaces reveals that the fracture always occurs in the adhesive (Fig. S5). This observation indicates that the adhesion strengths of all the Ni coatings are higher than ~60 MPa. Moreover, it can be reasonably considered that the true values of adhesion strengths of the C-Ni and E-Ni coatings should be higher than that of the GA-Ni coatings. Similar to the inter-particle bonding, surface protruding granules may generate more mechanical interlocking at the particle/substrate interface as compared with the smooth surface. In this study, due to the limited strength of commercial available adhesives, it is difficult to evaluate the contributions of surface protruding granules on the particle/substrate mechanical interlocking through routine tensile test. However, considering the adhesion strengths of widely used electroless Ni coatings are only ~10−20 MPa [23], the much higher adhesion strengths should ensure all the Ni coatings maintain structural integrity in normal service conditions. Therefore, in this study, the quality of coating/substrate interfaces bonding will not deteriorate the corrosion performance of the Ni coatings.

3.3. Corrosion protection performance

3.3.1. Electrochemical properties

Electrochemical measurements were used to investigate the corrosion behavior of the MF-CS Ni coatings during long-term immersion. Fig. 6 exhibits the E_{OCP} variations of all the coatings as a function of immersion time in 0.6 mol L^{-1} NaCl solution. For cathode coating/anode substrate such as Ni coating/Mg substrate in this work, local corrosion of the substrate surface will occur if the coating has through thickness gaps and this will result in lower E_{OCP} value than intrinsic E_{OCP} of the coating material. In this work, the E_{OCP} curve of the GA-Ni coating remains relatively stable during the entire immersion process and the potential stabilizes at - 0.28 VSCE after 200 h immersion, which is very close to that of the bulk Ni reported in literatures [15,23]. Note that the E_{OCP} value of the GA-Ni coatings still stabilizes at around - 0.29 VSCE even after 3000 h immersion, which clearly demonstrates that the GA-Ni coating is not aqueous solution permeable.

Different from the GA-Ni coating, E_{OCP} curves of both C-Ni and E-Ni coatings can be divided into three different stages: i) in the initial stage (4/10 h), the E_{OCP} values stabilize at around - 0.3 VSCE; ii) in the middle stage (4/10–170 h), the E_{OCP} values suddenly decrease to - 1.21 VSCE and continuously decrease towards negative potential; iii) in the last stage (> 170 h), the potentials finally stabilize at around - 1.50 VSCE, which are very close to the literature value of AZ31B Mg alloy immersed in neutral sodium chloride solutions [41–43]. The present result shows that the C-Ni and E-Ni coatings can only isolate corrosive media for no more than 4 h and 10 h, respectively. Furthermore, the final potential

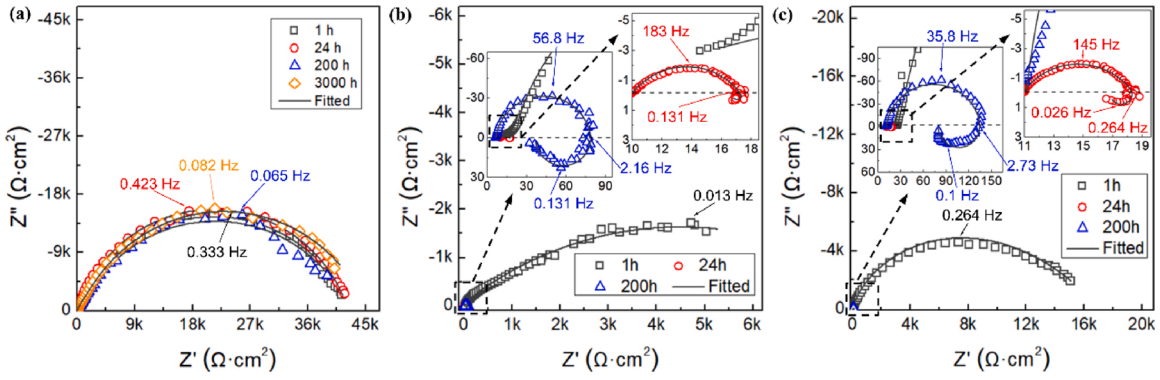

Fig. 7. Nyquist plots of the GA-Ni (a), C-Ni (b) and E-Ni (c) coatings at different corrosion stages in 0.6 mol L^{-1} NaCl aqueous solution.

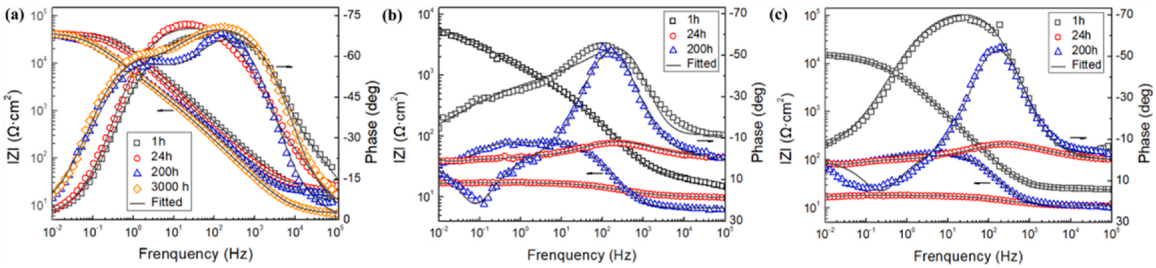

Fig. 8. Bode plots of the GA-Ni (a), C-Ni (b) and E-Ni (c) coatings at different corrosion stages in 0.6 mol L^{-1} NaCl aqueous solution.

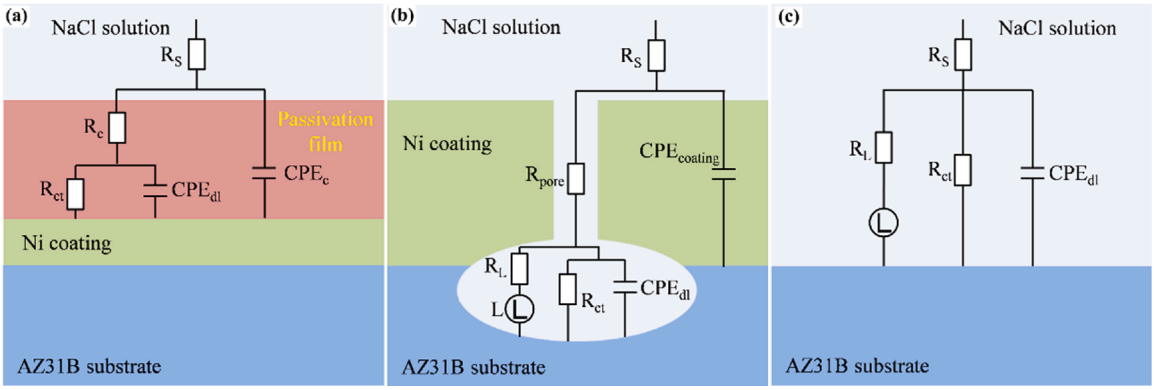

Fig. 9. Equivalent circuit models employed in fitting electrochemical impedance data.

stabilization suggests that the corrosion reactions of C-Ni and E-Ni coatings become steady in 0.6 mol L^{-1} NaCl solution.

To further understand the corrosion behaviors on different E_{OCP} stages, the EIS was measured when the samples were immersed in the 0.6 mol L^{-1} NaCl solution at 1, 24, 200 and 3000 h, respectively. EIS curves in Figs. 7 and 8 show the corrosion processes of the three Ni coatings in 0.6 mol L^{-1} NaCl solution. The solid fitting lines are plotted according to the equivalent circuit shown in Fig. 9. After 1 h immersion, the phase angles of the GA-Ni coating (Fig. 8a) show broad wave maxima close to - 75° at the middle and low-intermediate frequency, respectively. Therefore, the Nyquist plots of the GA-Ni coating in Fig. 7a should consist of two capacitive loops at the high and low frequency region, respectively. In literature [41], the capacitive loops in the middle and low-intermediate frequency are correlated with the characteristic of the electric double layer at electrode/electrolyte interface. Moreover, it can also be found that the EIS curves of the GA-Ni coating have no obvious change with the increase of immersion time (up to 3000 h), indicating a stable corrosion resistance in NaCl solution.

It is obvious that both the C-Ni and E-Ni coatings present different EIS curves at different corrosion stages. In the initial corrosion, both coatings present similar Bode and Nyquist plots as the GA-Ni coating, suggesting the same corrosion reaction occurred in the Ni coating side. However, the smaller capacitive loops of the C-Ni and E-Ni coatings still reveal a much higher corrosion rate as compared with the GA-Ni coating. In this work, as listed in Table 1, all the Ni powders contain similar elements with nearly the same content, so it is unlikely that the chemical composition difference would be the key explanation. Meanwhile, the relatively low deposition temperature in cold spray deposition process generates negligible chemical change (in the form of oxidation) during the coating deposition [32]. Thus, such a difference in corrosion rate probably mainly results from the higher fraction of inter-particle boundaries in the C-Ni and E-Ni coatings than that of the GA-Ni coating due to the smaller size or irregular morphology of sprayed particles. In our previous study [44], it was found that there are more crystal defects (e.g. dislocations) at the inter-particle boundaries due to their severe plastic deformation. During the corrosion process, the inter-particle boundaries in CS coating could act as active reaction zones for pitting corrosion [20]. Therefore, the higher fraction of inter-particle boundaries, the lower the corrosion resistance of CS coating. In the middle stage, the phase angles of both the coatings reveal a relaxation process with phase angle only close to -10° at the high-intermediate frequencies, suggesting a capacitive behavior with extremely poor dielectric properties. Moreover, the diameter of the capacitive loop in the Nyquist plot significantly decreases compared with that of initial corrosion, suggesting a worse corrosion resistance. This should be attributed to the galvanic corrosion of the AZ31B substrate in this corrosion stage. Meanwhile, the inductive loop at low frequencies in the fourth quadrant was initially observed in the Nyquist plot, which is the corresponding result of the corrosive pitting and film destruction of the corrosion products [5]. In the last stage, the diameters of the capacitive loops slightly increase, indicating a decreased galvanic corrosion rate. Besides, the inductive semicircle at low frequency becomes larger and more obvious. It may suggest that the accumulating the corrosion products on the surface and chemical reactions of corrosion products become more significant.

The equivalent circuit model is used to simulate the corrosion procedures of the GA-Ni coating as well as the curves of the C-Ni and E-Ni coatings in the initial stage as shown in Fig. 9a. In this way, R_s is the solution resistance, R_{ct} is the charge transfer resistance, CPE_{dl} is the constant phase element related to the inner electric double layer, CPE_c and R_c are the constant phase element and resistor of the Ni passivation film, respectively. The equivalent circuit depicted in Fig. 9b is usually used to simulate the EIS curves of the porous corrosion coatings after the corrosive media reach the substrate surface [45] (middle stage in this study). Apart from the R_s, R_{ct} and CPE_{dl}, the $CPE_{coating}$ is the constant phase element related to the coating and R_{pore} is the resistance of the electrolyte within the channel defects (through thickness gaps or cracks) of the coating. Meanwhile, since the inductive semicircle appears at low frequency in this stage (Fig. 8b-c), the R_L-L has a role in equivalent circuit, where R_L is the resistance of corrosion products and L is the inductive impedance resistance. At the last corrosion stage, the R_{pore}-$CPE_{coating}$ disappears in equivalent circuit shown in Fig. 9c, while this

Table 2
Calculated R values of the equivalent electrical circuit for the samples at different corrosion stages in 0.6 mol L^{-1} NaCl solution.

Samples	Immersion time (h)	R_s (Ohm cm^2)	R_{ct} (Ohm cm^2)	R_c (Ohm cm^2)	R_L (Ohm cm^2)	R_{pore} (Ohm cm^2)
C-Ni coating	1	14.9 ± 0.5	(6.7 ± 0.3) x 10^3	89 ± 3	–	–
	24	9.9 ± 0.7	7.1 ± 0.8	–	90 ± 3	0.32 ± 0.08
	200	6.5 ± 0.8	72 ± 3	–	52 ± 4	–
E-Ni coating	1	24 ± 2	(14.1 ± 0.5) x 10^3	79 ± 3	–	–
	24	11.0 ± 0.8	6.6 ± 0.3	–	71 ± 6	0.8 ± 0.1
	200	11 ± 1	125 ± 6	–	152 ± 12	–
GA-Ni coating	1	11 ± 1	(43 ± 1) x 10^3	32 ± 5	–	–
	24	19 ± 2	(42 ± 2) x 10^3	37 ± 5	–	–
	200	18 ± 1	(40.8 ± 0.7) x 10^3	46 ± 2	–	–
	3000	6.8 ± 0.7	(42 ± 2) x 10^3	68 ± 3	–	–

model is usually used to fit the EIS curve of Mg alloys [23,41].

The R values of the electric equivalent circuits obtained by fitting the experimental EIS data of the three proposed models are presented in Table 2. R_s is determined by the conductance of the 0.6 mol L^{-1} NaCl solution and according to these results, the solution resistance of all samples shows no significant difference. Generally, R_{ct} is an important parameter which directly represents the corrosion rate of the tested sample. During the whole immersion process, the average impedance values of the R_{ct} of the GA-Ni coating are stable at about 40 × 10^3 Ohm cm^2. This result reveals that the dissolution rates of the GA-Ni coatings in the neutral salt solution are extremely slow and stable. Similarly, the average R_{ct} values of the C-Ni and E-Ni coatings are attained to be 6.7 × 10^3 Ohm cm^2 and 14.1 × 10^3 Ohm cm^2 at the initial stage, respectively. However, these values are still much lower than that of the GA-Ni coating. This phenomenon should be associated with the fraction of inter-particle boundaries of CS coatings according to the previous explanation. As expected, the average R_{ct} values of the C-Ni and E-Ni coatings significantly reduce to 7.1 Ohm cm^2 and 6.6 Ohm cm^2, respectively, due to the galvanic corrosion effect in the middle stage. Note that the average resistance values of the pores in both coatings are less than 1 Ohm cm^2. This suggests that significant damage has occurred in the C-Ni and E-Ni coatings even only after 24 h. In the last corrosion stage, the average R_{ct} values of the C-Ni and E-Ni coatings slightly increase to ~ 100 Ohm cm^2. This value is similar to that of bare AZ31B alloy in literatures tested in similar conditions [41,42].

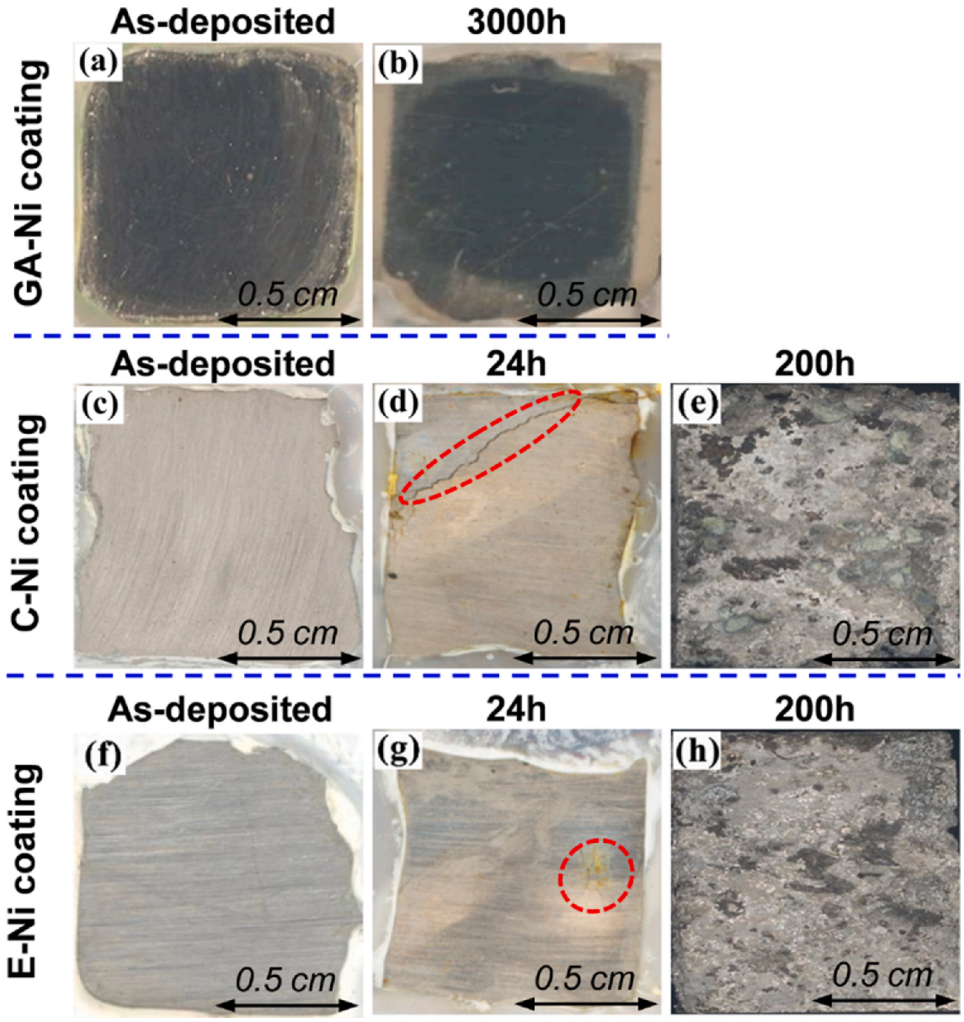

Fig. 10. The top surface appearances of the as-deposited and corroded GA-Ni (a and b), C-Ni (c to e) and E-Ni (f to h) coatings in 0.6 mol L^{-1} NaCl solution.

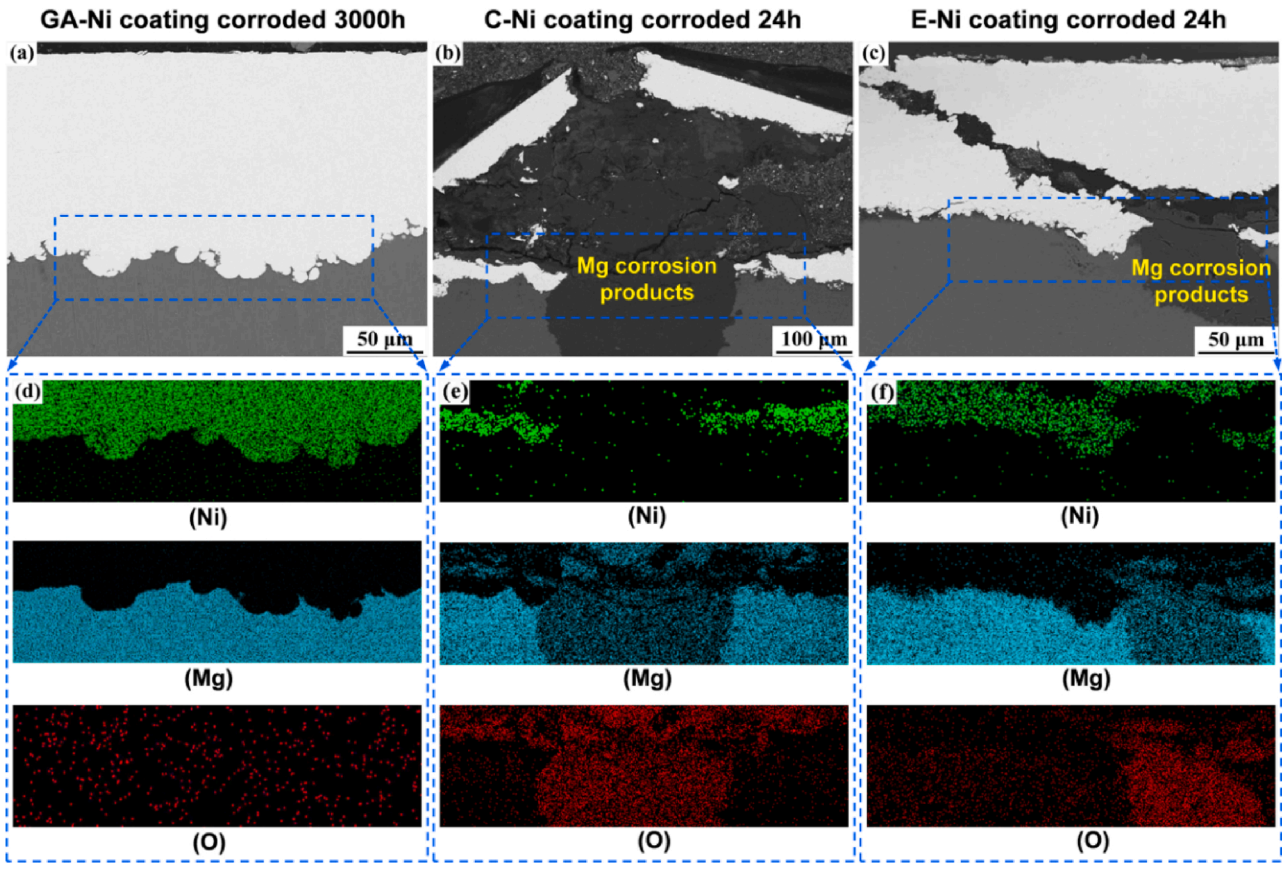

Fig. 11. The cross-sectional microstructures of the corroded GA-Ni (a), C-Ni (b) and E-Ni (c) coatings in 0.6 mol L^{-1} NaCl solution. (d)-(f) is the EDS elemental mapping of the marked area in (a)-(c), respectively.

3.3.2. Microstructure of the corroded coatings

Fig. 10 shows the top surface characteristics of the as-deposited and corroded Ni coating in 0.6 mol L^{-1} NaCl solution. The corroded sample surfaces were cleaned as per ASTM G1-03 [46] to remove the corrosion products. As presented in Fig. 10b, pitting and other localized corrosion were not observed on the surface of GA-Ni coating even after 3000 h immersion. As compared with the GA-Ni coating, macro-cracks (marked by dashed line ellipses in Fig. 10d and g) can be clearly observed on the surfaces of the C-Ni and E-Ni coatings only after 24 h immersion. After 200 h corrosion, the C-Ni (Fig. 10e) and E-Ni (Fig. 10h) coatings completely peeled off from the substrate. This explains why they present a similar corrosion behavior to that of bare AZ31B alloy in the last corrosion stage (Fig. 7b-c). Moreover, the AZ31B substrate presents very rough surface with many obvious corrosion pits, indicating the occurrence of severe corrosion.

Fig. 11 reveals the cross-sectional microstructures of the corroded Ni coating in 0.6 mol L^{-1} NaCl solution. As presented in Fig. 11a, the GA-Ni coating is still well bonded to the AZ31B substrate and no corrosion products were formed at the coating/substrate interface. This is further confirmed by the EDS results shown in Fig. 11d, which is based on the marked area in Fig. 11a. For the C-Ni and E-Ni samples (Fig. 11b-c), local corrosion products (with porous microstructures) which mainly compose of Mg and O elements (confirmed by EDS results in Fig. 11e-f) can be clearly observed on the AZ31B substrate surface after 24 h immersion. For these samples, the formation of porous corrosion products will result in local volume expansion and thereby tensile stress and crack initiation near the corroded areas. Therefore, the peel-off of C-Ni and E-Ni coatings mainly occurs near the corroded areas as displayed in Fig. 11b-c.

In sum, microstructural characterization of corroded coatings confirms that the GA-Ni coating is impermeable and presents excellent long-term corrosion protection for Mg alloys; while the C-Ni and E-Ni coatings fail only after several hours' immersion. Generally, the impermeability of cold sprayed coatings is often associated with the levels of coating defects, i.e. inter-connected porosity and inter-particle gap [34]. In this study, the Ni coatings are all dense and no obvious difference in porosity can be observed (Fig. 3a-c). The aforementioned results (Fig. 3d-f) illustrate that the GA-Ni coating presents an excellent inter-particle bonding (intimate contact interfaces), while many small inter-particle gaps can be observed in both the C-Ni and E-Ni coatings, which can act as fast pathways for in-depth penetration of corrosive solution. Therefore, the quality of inter-particle bonding is likely to be the contributing factor of different impermeabilities of the three MF-CS Ni coatings.

4. Conclusion

In this study, three different types of Ni powders, i.e. gas atomized Ni (GA-Ni),carbonyl Ni (C-Ni) and electrolytic Ni (E-Ni), were deposited onto the AZ31B Mg alloy by an in-situ micro-forging assisted cold sprayed (MF-CS) for corrosion protection. The resultant Ni coating microstructure, adhesion strength and corrosion performance were studied. Results show that although all Ni coatings have rarely visible pores and show comparable porosity level (<0.3 %), the C-Ni and E-Ni coatings reveal poorer inter-particle bonding than GA-Ni coating. Tensile tests indicate that the adhesion strengths of all the Ni coatings are higher than ~60 MPa. Corrosion tests reveal that the fully dense GA-Ni coating presents excellent long-term (3000 h) corrosion protection for Mg alloys, while the C-Ni and E-Ni coatings fail after only 10 h' immersion (corrosive media reach the coating/substrate interface through inter-particle gaps). In sum, although the GA-Ni powder incurs a higher production cost due to the relatively higher powder price and lower

deposition efficiency, it generates better corrosion protection performance than the C-Ni and E-Ni coatings via the MF-CS process. This work provides guidelines not only to select proper powder feedstock for cold spraying corrosion resistant coatings but also to properly evaluate the corrosion protection of the coatings.

Author statement

W.Y. Wei deposited the Ni coatings, characterized the microstructure, adhesion strength and corrosion performance of the coatings, and wrote the manuscript.

X. Chu and Y. Ge helped to deposit the Ni coatings.

Y.C. Xie and R.Z. Huang helped the corrosion tests.

X.T. Luo, G.S. Huang and C.J. Li designed the experimental programme, coordinated the overall project and provided research funding.

Data availability

The raw/processed data required to reproduce these findings cannot be shared at this time as the data also forms part of an ongoing study.

Declaration of Competing Interest

The authors declare that they have no known competing financial interests or personal relationships that could have appeared to influence the work reported in this paper.

Acknowledgments

This work is supported by National Natural Science Foundation of China (51875443), Research Fund of State Key Laboratory for Marine Corrosion and Protection of Luoyang Ship Material Research Institute (LSMRI).

Appendix A. Supplementary data

Supplementary material related to this article can be found, in the online version, at doi:https://doi.org/10.1016/j.corsci.2021.109397.

References

[1] M. Ali, M. Hussein, N. Al-Aqeeli, Magnesium-based composites and alloys for medical applications: a review of mechanical and corrosion properties, J. Alloys Compd. 792 (2019) 1162–1190, https://doi.org/10.1016/j.jallcom.2019.04.080.
[2] L.X. Li, Z.H. Xie, C. Fernandez, L. Wu, C.J. Zhong, Development of a thiophene derivative modified LDH coating for Mg alloy corrosion protection, Electrochim. Acta 330 (2019) 135186, https://doi.org/10.1016/j.electacta.2019.135186.
[3] X. Wang, D. Xu, R. Wu, X. Chen, Q. Peng, L. Jin, Y. Xin, Z. Zhang, Y. Liu, X. Chen, What is going on in magnesium alloys? J. Mater. Sci. Technol. 34 (2) (2018) 245–247, https://doi.org/10.1016/j.jmst.2017.07.019.
[4] A. Lelevic, F.C. Walsh, Electrodeposition of NiP alloy coatings: a review, Surf. Coat. Technol. 369 (2019) 198–220, https://doi.org/10.1016/j.surfcoat.2019.03.055.
[5] T. Zhang, G. Meng, Y. Shao, Z. Cui, F. Wang, Corrosion of hot extrusion AZ91 magnesium alloy. Part II: Effect of rare earth element neodymium (Nd) on the corrosion behavior of extruded alloy, Corros. Sci. 53 (9) (2011) 2934–2942, https://doi.org/10.1016/j.corsci.2011.05.035.
[6] H. Bu, M. Yandouzi, L. Chen, D. Macdonald, B. Jodoin, Cold spray blended Al+Mg17Al12 coating for corrosion protection of AZ91D magnesium alloy, Surf. Coat. Technol. 207 (2012) 155–162, https://doi.org/10.1016/j.surfcoat.2012.06.050.
[7] B.S. Deforce, T.J. Eden, J.K. Potter, Cold spray Al-5% Mg coatings for the corrosion protection of magnesium alloys, J. Therm. Spray. Technol. 20 (6) (2011) 1352–1358, https://doi.org/10.1007/s11666-011-9675-4.
[8] H. Assadi, H. Kreye, F. Gärtner, T. Klassen, Cold spraying–a materials perspective, Acta Mater. 116 (2016) 382–407, https://doi.org/10.1016/j.actamat.2016.06.034.
[9] Y. Tao, T. Xiong, S. Chao, L. Kong, X. Cui, T. Li, G.L. Song, Microstructure and corrosion performance of a cold sprayed aluminium coating on AZ91D magnesium alloy, Corros. Sci. 52 (10) (2010) 3191–3197, https://doi.org/10.1016/j.corsci.2010.05.023.
[10] M. Diab, P. Xin, H. Jahed, The effect of pure aluminum cold spray coating on corrosion and corrosion fatigue of magnesium (3% Al-1% Zn) extrusion, Surf. Coat. Technol. 309 (2016) 423–435, https://doi.org/10.1016/j.surfcoat.2016.11.014.
[11] Y. Tao, T. Xiong, S. Chao, H. Jin, D. Hao, T. Li, Effect of α-Al2O3 on the properties of cold sprayed Al/α-Al2O3 composite coatings on AZ91D magnesium alloy, Appl. Surf. Sci. 256 (1) (2009) 261–266, https://doi.org/10.1016/j.apsusc.2009.08.012.
[12] L.Y. Qin, Q.J. Jiang, L.Q. She, Effect of grain size on corrosion behavior of electrodeposited bulk nanocrystalline Ni, Trans. Nonferrous Met. Soc. China 20 (1) (2010) 82–89, https://doi.org/10.1016/S1003-6326(09)60101-1.
[13] C. Wang, C. Jiang, Z. Chai, M. Chen, L. Wang, V. Ji, Estimation of microstructure and corrosion properties of peened nickel aluminum bronze, Surf. Coat. Technol. 313 (2017) 136–142, https://doi.org/10.1016/j.surfcoat.2017.01.073.
[14] G. Kear, B. Barker, K. Stokes, F. Walsh, Electrochemical corrosion behaviour of 90—10 Cu—Ni alloy in chloride-based electrolytes, J. Appl. Electrochem. 34 (7) (2004) 659–669, https://doi.org/10.1023/B:JACH.0000031164.32520.58.
[15] H. Koivuluoto, J. Lagerbom, P. Vuoristo, Microstructural studies of cold sprayed copper, nickel, and nickel-30% copper coatings, J. Therm. Spray Technol. 16 (4) (2007) 488–497, https://doi.org/10.1007/s11666-007-9060-5.
[16] M. Scendo, W. Zorawski, A. Goral, Influence of nickel powders on corrosion resistance of cold sprayed coatings on Al7075 substrate, Metals 9 (8) (2019) 890, https://doi.org/10.3390/met9080890.
[17] F.S. da Silva, N. Cinca, S. Dosta, I.G. Cano, J.M. Guilemany, A.V. Benedetti, Cold gas spray coatings: basic principles, corrosion protection and applications, Eclética Química 42 (2017) 09–32, https://doi.org/10.26850/1678-4618eqj.v42.1.2017.p09-32.
[18] X.T. Luo, C.X. Li, F.L. Shang, G.J. Yang, Y.Y. Wang, C.J. Li, High velocity impact induced microstructure evolution during deposition of cold spray coatings: a review, Surf. Coat. Technol. 254 (2014) 11–20, https://doi.org/10.1016/j.surfcoat.2014.06.006.
[19] A. Pardo, P. Casajús, M. Mohedano, A. Coy, F. Viejo, B. Torres, E. Matykina, Corrosion protection of Mg/Al alloys by thermal sprayed aluminium coatings, Appl. Surf. Sci. 255 (15) (2009) 6968–6977, https://doi.org/10.1016/j.apsusc.2009.03.022.
[20] Y.K. Wei, X.T. Luo, Y. Ge, X. Chu, G.S. Huang, C.J. Li, Deposition of fully dense Al-based coatings via in-situ micro-forging assisted cold spray for excellent corrosion protection of AZ31B magnesium alloy, J. Alloys Compd. 806 (2019) 1116–1126, https://doi.org/10.1016/j.jallcom.2019.07.279.
[21] Y.K. Wei, X.T. Luo, X. Chu, G.S. Huang, C.J. Li, Solid-state additive manufacturing high performance aluminum alloy 6061 enabled by an in-situ micro-forging assisted cold spray, Mater. Sci. Eng. A 776 (2020) 139024, https://doi.org/10.1016/j.msea.2020.139024.
[22] Y.K. Wei, Y.J. Li, Y. Zhang, X.T. Luo, C.J. Li, Corrosion resistant nickel coating with strong adhesion on AZ31B magnesium alloy prepared by an in-situ shot-peening-assisted cold spray, Corros. Sci. 138 (2018) 105–115, https://doi.org/10.1016/j.corsci.2018.04.018.
[23] Y.K. Wei, Y.J. Li, Y. Zhang, X.T. Luo, C.J. Li, Corrosion resistant nickel coating with strong adhesion on AZ31B magnesium alloy prepared by an in-situ shot-peening-assisted cold spray, Corros. Sci. 138 (2018) 105–115, https://doi.org/10.1016/j.corsci.2018.04.018.
[24] V.N.V. Munagala, V. Akinyi, P. Vo, R.R. Chromik, Influence of powder morphology and microstructure on the cold spray and mechanical properties of Ti6Al4V coatings, J. Therm. Spray. Technol. 27 (5) (2018) 827–842, https://doi.org/10.1007/s11666-018-0729-8.
[25] S. Yin, P. He, H. Liao, X. Wang, Deposition features of Ti coating using irregular powders in cold spray, J. Therm. Spray. Technol. 23 (6) (2014) 984–990, https://doi.org/10.1007/s11666-014-0116-z.
[26] U. Prisco, Size-dependent distributions of particle velocity and temperature at impact in the cold-gas dynamic-spray process, J. Mater. Process Tech. 216 (2015) 302–314, https://doi.org/10.1016/j.jmatprotec.2014.09.013.
[27] L. Ajdelsztajn, B. Jodoin, J. Schoenung, Synthesis and mechanical properties of nanocrystalline Ni coatings produced by cold gas dynamic spraying, Surf. Coat. Technol. 201 (3-4) (2006) 1166–1172, https://doi.org/10.1016/j.surfcoat.2006.01.037.
[28] X. Chu, R. Chakrabarty, H. Che, L. Shang, P. Vo, J. Song, S. Yue, Investigation of the feedstock deposition behavior in a cold sprayed 316L/Fe composite coating, Surf. Coat. Technol. 337 (2018) 53–62, https://doi.org/10.1016/j.surfcoat.2017.12.063.
[29] X. Chu, H. Che, P. Vo, R. Chakrabarty, B. Sun, J. Song, S. Yue, Understanding the cold spray deposition efficiencies of 316L/Fe mixed powders by performing splat tests onto as-polished coatings, Surf. Coat. Technol. 324 (2017) 353–360, https://doi.org/10.1016/j.surfcoat.2017.05.083.
[30] D. Gilmore, R. Dykhuizen, R. Neiser, M. Smith, T. Roemer, Particle velocity and deposition efficiency in the cold spray process, J. Therm. Spray. Technol. 8 (4) (1999) 576–582, https://doi.org/10.1361/105996399770350278.
[31] T. Schmidt, F. Gärtner, H. Assadi, H. Kreye, Development of a generalized parameter window for cold spray deposition, Acta Mater. 54 (3) (2006) 729–742, https://doi.org/10.1016/j.actamat.2005.10.005.
[32] X.-T. Luo, Y.-J. Li, C.-X. Li, G.-J. Yang, C.-J. Li, Effect of spray conditions on deposition behavior and microstructure of cold sprayed Ni coatings sprayed with a porous electrolytic Ni powder, Surf. Coat. Technol. 289 (2016) 85–93, https://doi.org/10.1016/j.surfcoat.2016.01.058.
[33] G. Bae, J.I. Jang, C. Lee, Correlation of particle impact conditions with bonding, nanocrystal formation and mechanical properties in kinetic sprayed nickel, Acta Mater. 60 (8) (2012) 3524–3535, https://doi.org/10.1016/j.actamat.2012.03.001.
[34] Y. Xiong, G. Bae, X. Xiong, C. Lee, The effects of successive impacts and cold welds on the deposition onset of cold spray coatings, J. Therm. Spray. Technol. 19 (3) (2010) 575–585, https://doi.org/10.1007/s11666-009-9455-6.
[35] X.T. Luo, Y. Ge, Y. Xie, Y. Wei, R. Huang, N. Ma, C.S. Ramachandran, C.J. Li, Dynamic evolution of oxide scale on the surfaces of feed stock particles from

cracking and segmenting to peel-off while cold spraying copper powder having a high oxygen content, J. Mater. Sci. Technol. 67 (2021) 105–115, https://doi.org/10.1016/j.jmst.2020.06.019.
[36] ASTM C633-13, Standard Test Method for Adhesion or Cohesion Strength of Thermal Spray Coatings, ASTM International, West Conshohocken, PA, 2017, https://doi.org/10.1520/C0633-13R17.
[37] X.T. Luo, Y.K. Wei, Y. Wang, C.J. Li, Microstructure and mechanical property of Ti and Ti6Al4V prepared by an in-situ shot peening assisted cold spraying, Mater. Des. 85 (2015) 527–533, https://doi.org/10.1016/j.matdes.2015.07.015.
[38] J. Jungk, B. Boyce, T. Buchheit, T. Friedmann, D. Yang, W.W. Gerberich, Indentation fracture toughness and acoustic energy release in tetrahedral amorphous carbon diamond-like thin films, Acta Mater. 54 (15) (2006) 4043–4052, https://doi.org/10.1016/j.actamat.2006.05.003.
[39] D. Goldbaum, J. Ajaja, R.R. Chromik, W. Wong, S. Yue, E. Irissou, J.-G. Legoux, Mechanical behavior of Ti cold spray coatings determined by a multi-scale indentation method, Mater. Sci. Eng. A 530 (2011) 253–265, https://doi.org/10.1016/j.surfcoat.2016.11.014.
[40] K.S. Al-Hamdani, J.W. Murray, T. Hussain, A.T. Clare, Heat-treatment and mechanical properties of cold-sprayed high strength Al alloys from satellited feedstocks, Surf. Coat. Technol. 374 (2019) 21–31, https://doi.org/10.1016/j.surfcoat.2019.05.043.
[41] R. Gan, D. Wang, Z.-H. Xie, L. He, Improving surface characteristic and corrosion inhibition of coating on Mg alloy by trace stannous (II) chloride, Corros. Sci. 123 (2017) 147–157, https://doi.org/10.1016/j.corsci.2017.04.018.
[42] C. Xie, H. Li, X. Zhou, C. Sun, Corrosion behavior of cold sprayed pure zinc coating on magnesium, Surf. Coat. Technol. 374 (2019) 797–806, https://doi.org/10.1016/j.surfcoat.2019.06.068.
[43] Y. Xin, J. Zimin, L. Linxin, X. Zhi-Hui, In-situ growth of NiAl-Layered double hydroxide on AZ31 Mg alloy towards enhanced corrosion protection, Nanomaterials 8 (6) (2018) 411, https://doi.org/10.3390/nano8060411.
[44] X.T. Luo, C.J. Li, Tailoring the composite interface at lower temperature by the nanoscale interfacial active layer formed in cold sprayed cBN/NiCrAl nanocomposite, Mater. Des. 140 (2018) 387–399, https://doi.org/10.1016/j.matdes.2017.11.062.
[45] S. Mirhashemihaghighi, J. Światowska, V. Maurice, A. Seyeux, L.H. Klein, E. Salmi, M. Ritala, P. Marcus, Interfacial native oxide effects on the corrosion protection of copper coated with ALD alumina, Electrochim. Acta 193 (2016) 7–15, https://doi.org/10.1016/j.electacta.2016.02.014.
[46] ASTM G1-03, Standard Practice for Preparing, Cleaning, and Evaluating Corrosion Test Specimens, ASTM International, West Conshohocken, PA, 2017, https://doi.org/10.1520/G0001-03R17E01.